Supplementary Material for

A largely invariant marine dissolved organic carbon reservoir across Earth's history

1. The box model

The box model for marine dissolved organic carbon (DOC) includes eight oceanic boxes: shallow/continental shelf, surface, intermediate, deep, downwelling high-latitude, upwelling high-latitude, upwelling slope, and upwelling surface (Fig. 1). The geometric details of the boxes are presented in Table S1. DOC is transported between oceanic regions through physical transport. The major physical transport mechanisms are diffusional exchange caused by turbulence, Ekman (wind-driven) upwelling, thermohaline circulation caused by density and salinity gradients, and advective riverine flux.

The concentration of DOC in each oceanic box is calculated by solving the following differential equation:

$$V_i \frac{dC_i}{dt} = F_{Physical} + F_{Chem} \quad (1)$$

where C_i is the concentration of dissolved organic carbon in box i, $F_{Physical}$ corresponds to the sum of all physical transport fluxes, and F_{Chem} is the sum of all biotic and abiotic chemical reactions that produce or consume DOC.

As an example, the change in DOC concentrations in the continental shelf, Box 1, is calculated as follows:

$$\frac{dDOC_1}{dt} = F_{POC-DOC} - F_{DOC-DIC} - F_{Photo} + F_{Physical} \quad (2)$$

Where $F_{POC\text{-}DOC}$, $F_{DOC\text{-}DIC}$, F_{Photo}, $F_{Physical}$ denote, respectively, the fluxes of DOC production from POC, DOC transformation into DIC, photodegradation of DOC, and the sum of all the physical transport fluxes into and out of the box. The rate of physical transport of different species between boxes is calculated as follows:

$$F_{Physical,ij} = K_{ij}\left(C_i - C_j\right) \quad (3)$$

where K_{ij} represents transport kinetics between the oceanic box "*i*'' and its adjacent box "*j*''. C_i and C_j are, respectively, the concentration of dissolved species in boxes *i* and *j*.

2. Modeling the marine biological pump

An important component of the marine DOC cycle is the marine biological pump (MBP). To explore the effect of changes in the biological structure of the MBP (e.g., the rise of eukaryotic algae, and of fecal-pellet producing zooplankton) on the marine DOC pool, we coupled our ocean-atmosphere box model to a previously developed particle aggregation model (1). Briefly, the particle model couples stochastic particle aggregation and transport with temperature- and oxygen-dependent organic matter remineralization. Aggregates, the constitutive elements of the model, are clusters of phytoplankton cells (e.g., diatoms, non-skeletal algae, picoplankton, zooplankton) and terrigenous dust particles. In the uppermost layer of the ocean, we stochastically 'seed' a stock of primary particles based on assumed primary productivity of picoplankton and algal biomass, algal calcite flux, and surface dust flux. These particles then sink from the surface ocean and interact in the ocean interior through aggregation/disaggregation and organic matter respiration. To account for spatial heterogeneity, the model calculates the sinking rates of a large number of aggregates

(10^6) at each depth layer. Dividing the ocean into 1000 depth intervals results in 10^9 potential aggregates.

In the ocean interior, particle aggregation is controlled by the particle collision rate and a particle aggregation efficiency parameter ('stickiness,' γ; cf. 2). For the aggregation parameterization scheme, the number of particles at each depth is determined by a calculated aggregation rate. The probability of aggregation between two aggregates *i* and *j* ($P_{i,j}$) is defined as:

$$P_{i,j} = \gamma(z).\frac{\beta(i,j)}{\beta_{ref}}.\frac{F_{NPP}(z)}{F_{NPP_{ref}}}.\frac{F_{dust}(z)}{F_{dust_{ref}}} \quad , \qquad (4)$$

where β is the rate of collision between aggregates *i* and *j*, γ is the aggregation efficiency parameter that varies with depth, F_{NPP} and F_{dust} are the fluxes of net primary production and dust, respectively; and β_{ref}, $F_{NPPref,}$ $F_{dustref}$ are the reference values for collision rate, the flux of net primary production, and dust flux, respectively. The last two parameters in the expression for the probability of aggregation ($F_{NPP}/F_{NPPref,}$ $F_{dust}/F_{dustref}$) represent the higher probability of collision between aggregates at higher overall fluxes of primary particles from photosynthetic production and dust. The aggregation efficiency parameter (γ) is defined to decrease with depth, similar to the rate of organic matter degradation (following 3). This assumption is based on observations of modern marine systems, where the primary substrate that holds marine snow together in the water column is transparent exopolymer particles (TEP)—a mucus-like polysaccharide material exuded by phytoplankton and bacteria. It has been suggested that production of these compounds is highest under conditions of nutrient limitation during the senescent phase of phytoplankton blooms (2).

The overall rate of collision between two particles, β, is controlled by three mechanisms: very small particles mostly encounter each other by Brownian motion, whereas large particles meet

each other due to fluid shear and differential settling (i.e., the larger particles settle faster, sweeping up the smaller ones). In our model, similar to previous models (2), the coagulation kernel β is calculated as a sum of these three mechanisms: collision frequency due to Brownian motion (4, 5):

$$\beta_{Br} = \frac{8kT}{6\mu}\frac{(r_i+r_j)^2}{r_i r_j}, \quad (5)$$

fluid shear:

$$\beta_{sh} = 9.8\frac{q^2}{1+2q^2}\sqrt{\left(\frac{\varepsilon}{\nu}\right)}\left(r_i + r_j\right)^3, \quad (6)$$

where q = MIN (r_i , r_j) / MAX (r_i , r_j), and differential settling:

$$\beta_{ds} = \frac{1}{2}\pi\, MIN\left(r_{i\,,}\, r_j\right)^2\left|u_i - u_j\right| \quad (7)$$

Here k is the Stefan– Boltzman constant, μ is dynamic viscosity, v is kinematic viscosity and ε is the turbulent dissipation rate set to 1×10^{-4} (ref. 2), whereas r_i and r_j are the radii of the two aggregates being evaluated for collision, and u_i and u_j are the settling velocities of the two aggregates.

The averaged probability of aggregation at each depth is then used to determine the proportion of particles that are incorporated into aggregates in the following depth. For instance, at the very top of our domain where there is no aggregation, primary interacting particles (e.g., picoplankton, dust, etc.) are evaluated for aggregation, and the average probability of aggregation at that depth is evaluated and used to determine what percentage of particles in the following depth will be contained within an aggregate.

Aggregate sinking rates are calculated using Stokes' Law (6):

$$u = \sqrt{\frac{8r_a(\rho_a - \rho_{sw}).g}{3\rho_{sw}f(Re)}} \quad (8)$$

where g is the gravity of Earth. For low Reynolds numbers where viscous forces are dominant,

$$f(Re) = \frac{24}{Re} \text{ and } Re = \frac{2r_a u}{\nu} \quad (9)$$

For large Reynolds numbers where turbulence starts to play a role, the drag coefficient is calculated using Whites' approximation:

$$f(Re) = \frac{24}{Re} + \frac{6}{(1+\sqrt{Re})} + 0.4\,, \quad (10)$$

which is valid for Re < 2×10^4 (7). Calculated average velocity at each depth is used to obtain the organic matter age depth profile:

$$t_{age} = \frac{z_i}{u_{i,average}}\,, \quad (11)$$

Where z_i corresponds to depth (in meters) and $u_{i,average}$ is the average velocity of aggregates at depth i (in meters/day).

2.1. The role of zooplankton

The model also accounts for the interaction between marine aggregates and zooplankton. Zooplankton in the model are grouped into small and large zooplankton based on their prosome length and their corresponding behavior. Small zooplankton in the model interact with oceanic aggregates and can either fragment aggregates, generating smaller-sized aggregates, or ingest them

and produce a range of fecal pellets sizes as a function of their prosome length. Observations of the modern ocean indicate that particle aggregation plays an important role in POC flux attenuation in the ocean mesopelagic zone (8). Specifically, evidence of the slow sinking of oceanic aggregates in the modern deep ocean suggests that disaggregation/fragmentation of aggregates contributes substantially to the operation of the marine biological pump (8). It has been suggested that fragmentation is mainly caused by turbulent flow in the ocean. However, experimental studies of marine aggregates have revealed that larger stresses in excess of those due to turbulent shear in the ocean are needed to break the aggregates, suggesting that fragmentation caused by biological shear is the main control on aggregate fragmentation in the ocean (9). This finding is also consistent with the observed decrease in the average size of marine particle aggregates where the zooplanktonic crustacean *Euphausia pacifica* is abundant (10). While the degree to which zooplankton influence the physical characteristics of marine particle aggregates is not fully understood, experimental and modeling studies confirm that interaction between zooplankton and marine particles occurs and can lead to aggregate fragmentation. However, aggregate destruction is restricted to particular clades of zooplankton, such as copepods. Other common types of zooplankton, like salps, are predicted to induce minimal fragmentation (11).

Large zooplankton in the model are further categorized as migrating and non-migrating zooplankton. The migrating zooplankton represent those members of the zooplankton community that are able to vertically migrate through the ocean twilight zone during the day and night, a process that is commonly known as diel vertical migration (DVM), with consequent impacts on POC flux and vertical carbon transfer. Generally, DVM is a movement of zooplankton to the twilight zone during the day and back to shallower and more surficial waters during the night.

There are a number of environmental factors that have been suggested to impact the DVM, including water clarity, oxygen availability, seawater surface temperature, turbulence, and predator-prey interactions (12, 13). Modern observations indicate that DVM accounts for between 10 and 50% of the total vertical flux of carbon from shallow waters, suggesting that DVM plays an important role in transferring fixed carbon into the ocean mesopelagic zone (14). In the model, we first evaluate the possibility of zooplankton encountering marine particle aggregates and then, depending on the zooplankton class, the aggregates can be fragmented (disaggregated) or ingested and produce a range of fecal pellet sizes. The calculated POC flux is then corrected to account for the effect of DVM (1).

2.1.1. Encounter rate between marine aggregates and zooplankton

While the encounter rate between aggregates and zooplankton is not well constrained, we adapt for this purpose the expression for the encounter rate of predator-prey interactions in zooplankton (15). In the modern ocean the encounter rate for predator and prey is suggested to be governed by two main processes: behavioral locomotion, E_B, and physical transport (e.g., turbulence), E_T. The former process reflects the effect of predator ability to autonomously move (swimming), whereas the latter process is a hydrodynamic process which can be further divided into floating and turbulent mixing processes, both of which impact aggregation and the relative speed of the predator with respect to its prey. Thus, the overall encounter rate can be expressed as:

$$E = E_B + E_T \quad . \tag{12}$$

Under the assumption that the speed of the predator, v, exceeds that of the prey, u, E_B is parameterized as (16):

$$E_B = \pi Z_p d^2 \frac{u^2+3v^2}{3v} \quad , \tag{13}$$

where *d* is the zooplankton contact radius (i.e., the maximum distance at which the zooplankton can perceive the aggregate), and Z_P is the aggregate concentration. Encounter rate as a result of turbulent mixing can also be expressed as (15):

$$E_T = \pi Z_p d^2 w \quad , \tag{14}$$

where *w* is the linear orbital velocity of turbulent eddies (the turbulent velocity).

E_B corresponds to the behavioral impact on the encounter rate and E_T relates the effect of turbulent mixing to the encounter rate. To account for the contribution of microscale turbulence to the relative motion of predator and prey, the original encounter rate equation was revised, and the overall encounter rate recast as (15):

$$E = \pi Z_p d^2 \frac{u^2+3v^2+4w^2}{3(v^2+w^2)^{0.5}} \quad , \tag{15}$$

In our model, the encounter rate is defined as the ratio of the encounter rate calculated for each aggregate velocity, u_i, divided by the encounter rate calculated using the typical range of values (zooplankton speed, *v*; turbulence, *w*; and the aggregate velocity, *u*) for the modern ocean. Assuming a relatively constant contact radius, *d*, for the modern and ancient oceans, the encounter rate can then be expressed as:

$$E_{total} = \frac{Z_{p_1} \frac{u_i^2+3v^2+4w^2}{3(v^2+w^2)^{0.5}}}{Z_p \frac{u^2+3v^2+4w^2}{3(v^2+w^2)^{0.5}}} \quad , \tag{16}$$

where Z_{p1} is the aggregate concentration in the ancient ocean. We assume that aggregate concentration, Z_p, is controlled by the strength of net primary production, and high net primary

production results in higher aggregate concentrations. Equating the ratio of Z_p to the ratio of net primary production in the modern and ancient oceans ($Z_p/Z_{p1} = F_{NPP}/F_{NPPref}$), and assuming constant values for *v* and *w* throughout geologic time, the encounter rate can be rewritten as:

$$E_{total} = \frac{u_i^2+3v^2+4w^2}{u^2+3v^2+4w^2} \cdot \frac{F_{NPP}}{F_{NPPref}} \quad (17)$$

Values of *v* and *w* are randomly sampled from the range suggested for the modern ocean (Table S2). We chose different ranges of *v* for different classes of zooplankton in the model (small and large; Table S2).

The typical aggregate velocity, *u*, for the modern ocean covers a wide range and has been found to exhibit a bimodal distribution, with a substantial concentration of values close to 1 m/day and 1000 m/day, but very few aggregates with settling velocities between these values (17, 18). The *u* in our model takes values between 10 and 1000 m/day and is truncated to this range for aggregates that fall above or below these values. The value of E_{total} is between 0 and 1, and if its value in rare cases (e.g., higher calculated aggregate velocity, u_i, than the typical value, *u*) exceeds 1, the value of E_{total} is set to 1. The calculated encounter rate is then compared to a randomly generated value, *r*, and if $r < E_{total}$, the zooplankton encounter and either ingest or fragment the aggregate.

2.1.2. Fragmentation

To determine whether the aggregates encountered by zooplankton are fragmented or ingested, our model first evaluates the likelihood of fragmentation. Assuming that the probability of breaking larger particles is higher than that of breaking smaller ones, the parameter R_{break} increases as the aggregate radius increases. Similar to previous work (2), we define R_{break} as:

$$R_{break} = 0.1 \tan^{-1}(r_a/10^4) \quad , \quad (18)$$

where r_a is the aggregate radius, as described above. If a randomly generated value, *r*, is smaller than R_{break}, the aggregate fragments into a number of daughter particles. Following previous work (2) we use a power law with support between 2 and 24 integers (fragments) that describes the number of fragments, *f*, into which an aggregate can fragment:

$$P_f = \sum_{i=2}^{f} 0.91.i^{-1.56} \quad . \quad (19)$$

A randomly generated value, *r*, is compared to the value of P_f for each successive *f* starting from 2. When $r < P_f$, the number of fragments that the aggregate breaks into is obtained. The radius of the fragmented aggregate is then calculated by dividing the old radius by the number of fragments, *f*.

Recent observations indicate variation with depth in the efficiency of particle fragmentation by zooplankton, with elevated fragmentation in shallower parts of the ocean mesopelagic zone and attenuated fragmentation with increasing depth (19). To account for depth variation in the efficiency of fragmentation, we modified the R_{break} values according to a power-law function ($f_{frag} = k_{frag} \cdot z^{-0.258}$; where k_{frag} is between 0.1 and 1) that mimics the observed depth profile of fragmentation rate with the maximum value of 1 at 200 m (14).

Not all zooplankton have the same efficiency in fragmenting marine aggregates, and there are even some species that ingest aggregates and produce fecal pellets but do not actively fragment aggregates (e.g., salps; 11). To take into account such variation in the efficiency of particle

fragmentation (including no fragmentation) for some zooplankton, we varied the value of k_{frag} between 0.1 and 1.

2.1.3. Ingestion

If the particle is not fragmented, it is ingested and can produce fecal pellets. To ensure that zooplankton do not ingest aggregates without organic matter, a randomly generated value, r, is compared to the organic weight fraction (f_{org}) of each aggregate and if $r < f_{org}$, the aggregate is considered to be ingestible. Ingestion of aggregates by zooplankton results in a range of fecal pellet sizes. Fecal pellets are treated by the model essentially as lower-porosity aggregates as they are more compact than other aggregates, between 43 and 65% porosity (20). The size of fecal pellets produced in any single interaction is determined through random selection, assuming a uniform distribution. The range of values for fecal pellet size is obtained from the relationship between mean fecal pellet volume and prosome length for copepods (21):

$$log\ PV = 2.58\ log\ PL - 2.38 \quad , \tag{20}$$

where PV and PL represent the pellet volume and prosome length, respectively. To account for a range of sizes in different zooplankton classes (small vs. large), we assume ranges of prosome lengths (Table S2).

2.1.4. Effect of diel vertical migration (DVM)

To explore the effect of DVM on POC, we assume that a portion of the produced organic matter in the epipelagic zone is transferred into the mesopelagic zone by zooplankton through DVM, which reduces the available organic matter at the surface while transferring fresh organic matter to depth. The total amount of organic carbon in the mesopelagic zone can be expressed as:

$$C_{total} = C_{DVM} + C_{NDVM} \quad , \quad (21)$$

where C_{DVM} and C_{NDVM} are, respectively, the amount of organic matter transferred through DVM and the amount of organic matter transferred through the background sinking POC flux. C_{DVM} is also estimated as the concentration of POC at the surface multiplied by a factor, K_{DVM}, that specifies the percentage of organic matter content at the surface that is transferred through DVM. We varied K_{DVM} between 5 and 40%, and the range of depth within which organic matter is transferred through DVM is varied between 300 and 800 meters. While relatively simple, this parameterization allows us to investigate the effect of the evolution of large zooplankton with the ability to conduct DVM on marine POC flux, burial efficiency, and oxygen dynamics.

3. Rate of carbon degradation and mineralization

As described in the main-text Methods, the results of an organic-matter age-depth profile resulting from the particle model were used to calculate the integrated depth profile for carbon degradation and mineralization in each oceanic box. Mechanistically, as marine particle aggregates sink through the water column, POC (e.g., biopolymers) with high molecular weights (HMW; >>1000 Dalton) are degraded and depolymerized into smaller organic molecules with lower molecular weights (e.g., DOC) (22). The resultant DOC is then further degraded and mineralized, which results in the generation of inorganic carbon (DIC) (22). The overall rate of carbon transformation from POC to DIC is controlled by the rate of each degradation step. While the mechanisms controlling the rate of the multi-stage conversion of organic matter to inorganic carbon are not fully understood, we use a well-established power-law framework for organic matter degradation (23). Using this power-law function for the carbon degradation rate, the rate of POC transformation into DOC can then be expressed as:

$$R_{POC\text{-}DOC} = -bt^{-a}C \quad , \tag{22}$$

where C is the concentration of organic matter as POC, and the constants a and b define the rate of organic carbon mineralization. This empirical power law has been found to hold over a wide range of organic matter degradation timescales, ranging from fresh phytoplankton to sedimentary organic matter buried millions of years ago (23, 24).

However, this relationship does not account for the effects of temperature, dissolved oxygen concentrations, mineral matrix properties, or other factors that likely also impact rates of carbon degradation (22, 25, 26). In particular, differences between organic carbon reactivities in oxic versus anoxic conditions (27) strongly influence the efficiency of carbon burial on geological time scales (25, 28). To explore the effect of oxygen on the marine carbon pump, we employ a modified power law (24) in which different a and b values are used to account for the differential reactivity of organic matter in oxic vs. anoxic settings (24). While there is uncertainty involved in estimating the power-law coefficients under oxic vs. anoxic conditions, experimental and statistical studies confirm that organic matter degradation rates are enhanced under oxic conditions (e.g., 24, 29, 30). To better account for the uncertainty associated with estimating power-law coefficients under oxic and anoxic conditions, we fit the carbon degradation power law to the measured depth profile of POC flux in modern oxic ocean waters (Figure 2).

We further modify the carbon degradation rate, following ref. 31–33, by adding a temperature dependency factor, Q_{10}, which for most biological systems is somewhere between 1.5 and 2.5 (32, 33):

$$R_{POC-DOC} = Q_{10}^{\frac{T-T_{ref}}{10}} . -bt^{-a}C \quad , \tag{23}$$

where T is the ambient environmental temperature and T_{ref} is a reference temperature. Parameter C is the concentration of organic matter as POC, and the constants a and b define the rate of organic carbon mineralization. The rate of DOC production from POC is then integrated over a given depth range corresponding to each oceanic box in the ocean-atmosphere box model.

Since the rate of the terminal mineralization step, where DOC is converted to DIC, is a function of both the size and reactivity of the POC pool available at each oceanic depth, the integrated rate of DOC uptake in each oceanic box can be expressed by a Monod scheme. Such formulation is supported by experimental and modeling studies (34, 35):

$$F_{DOC-DIC} = \alpha . R_{POC-DOC} . \frac{[DOC]}{k_{DOC}+[DOC]} . A_i \quad , \tag{24}$$

where $R_{POC\text{-}DOC}$ is the depth-integrated rate of conversion of POC to DOC, calculated using the power law described above; [*DOC*] is the concentration of DOC in each oceanic box; k_{DOC} is the half-saturation constant for DOC degradation; A_i is the area of the corresponding oceanic box; and α is the fitting parameter obtained by fitting the DOC depth profile from our model to the measured depth profile in the modern ocean. Mechanistically, the factor k_{DOC} represents the impact of the "dilution hypothesis" in which a low DOC concentration is invoked to explain large deep-ocean DOC storage (34). The value of k_{DOC} has been suggested to be approximately 231.16 ± 899.99 µM (Table S1) (36).

To account for the uncertainty involved in estimating the oceanic DOC pools, we use a stochastic approach. In short, model parameters were randomly sampled within their expected ranges (based on current literature estimates), assuming a uniform prior distribution (Table S1). To validate our model assumptions, we compared our model to empirical data from three different modern settings: the oxic ocean, the anoxic and sulfide-rich Black Sea, and the anoxic and iron-rich freshwater Lac Pavin, France. Each of these environments was selected to represent various endmembers for marine redox states characteristic of Earth's past. While the assumptions for DOC generation and consumption for the modern ocean, Black Sea, and Lac Pavin are the same, we modified the box model to account for the different physical structures and transport in the Black Sea and Lac Pavin. Specifically, we considered a two-box model, instead of eight boxes, for the Black Sea and Lac Pavin. The surface box in the Black Sea includes DOC influx from the Danube River, which today accounts for more than 65% of riverine water discharge and outflow to the Bosphorus (37). The exchange of mass between the surface box and the deep box occurs through vertical eddy diffusivity. The deep box receives DOC from the surface waters through vertical diffusion, with DOC flux from the deep sediments. Similar to the Black Sea, we simulated the DOC distribution in the anoxic and iron-rich freshwater Lac Pavin, France, with two boxes representing surface and deep waters. DOC under this scenario is generated through heterotrophic degradation of POC in the surface waters and the exchange of DOC with deep water is mediated by vertical eddy diffusivity (38). In addition to the exchange flux of DOC from the surface box, the deep box in Lac Pavin is considered to receive DOC from sediment. The sediment benthic flux of DOC was obtained by considering Fick's diffusion law using bottom water concentration of DOC, and DOC molecular diffusion coefficient (39). Overall this exercise demonstrates consistency between the modeled DOC and the observed DOC in these environments, suggesting

that the model can be used to explore the change in DOC concentrations under various chemical and biological conditions (Fig. 2).

4. Sensitivity analyses

To investigate the sensitivity of our results to the values of individual box model parameters, we conducted a suite of sensitivity analyses. The model parameters were varied within their reasonable ranges (specified in Table S1), and associated changes in average DOC concentration were recorded (Fig. S1). The effect of each model parameter on DOC concentration was normalized so that the comparison between the model parameters could be made conveniently. The primary conclusion presented in the main text—that the overall size of the marine DOC reservoir has very likely been largely static throughout Earth's history—is essentially insensitive to variation of most of the model input parameters, including benthic flux of DOC in coastal and deep sediments and riverine and hydrothermal fluxes of DOC. In contrast, we found that the half-saturation constant for DOC uptake (k_{DOC}) and the fitting parameter α (Fig. S1) strongly impact marine DOC concentrations. Notably, increasing k_{DOC} would result in a decrease in the rate of DOC uptake by heterotrophs, which in turn would allow the accumulation of DOC in the deep oceans. It is, however, not clear that k_{DOC} would have undergone substantial changes through Earth's history. The fitting parameter "α", as another parameter that has a rather strong influence on the steady-state concentration of DOC in the model, reflects the higher biodegradability of DOC compared to POC and is considered to vary between 2 and 10, meaning that the rate of DOC degradation is between 2 to 10 times higher than the rate of POC degradation. This value is, indeed, dependent upon the environmental and biological factors and can be different for each

environment. To account for the uncertainty involved with the choice of this value, we considered the full range of 2-10 in our stochastic analysis.

Given the uncertainty involved with estimating atmospheric oxygen levels and the evolutionary timing of the emergence and radiation of algal phytoplankton in marine ecosystems, we performed simulations under two different atmospheric oxygen levels of 0.01 and 0.1 PAL, under differing contributions of algae to marine primary production. Our results indicate that our modeled marine DOC concentrations are statistically indistinguishable under different atmospheric oxygen levels and with different contributions of algae to marine primary production (Fig. S2). This result can be explained by the fact that the POC flux resulting from our biological pump model is not sensitive to differences between high- and low-algae conditions.

Our results indicate that the main mechanisms that control the deep-ocean DOC reservoir are the effect of DOC uptake threshold (k_{DOC}), representing the "dilution hypothesis" (34), and the strength of oceanic circulation (Fig. S3 and S4). Notably, our results indicate that increasing the k_{DOC} value can increase the steady-state DOC concentration in the deep ocean to >100 μM, about three times higher than its current minimum value (~35 μM) (Fig. S3). Changes to ocean circulation can also influence DOC dynamics in the deep ocean. Specifically, an order of magnitude decrease in the strength of oceanic circulation can lead to about 10 μM reduction in the steady-state DOC concentration in the deep-ocean box (Fig. S4). This result underscores the important role of oceanic circulation in controlling the deep-ocean DOC reservoir. Taken together, while a change in the efficiency of oceanic circulation might have modulated the deep-ocean DOC pool, change

in the DOC uptake threshold—which depends on the physiology of marine heterotrophs—appears to exert the most leverage on the deep-ocean DOC reservoir.

References:

1. M. Fakhraee, N. J. Planavsky, C. T. Reinhard, The role of environmental factors in the long-term evolution of the marine biological pump. *Nat. Geosci.* **13**, 812–816 (2020).

2. T. Jokulsdottir, D. Archer, A stochastic, Lagrangian model of sinking biogenic aggregates in the ocean (SLAMS 1.0): Model formulation, validation and sensitivity. *Geosci. Model Dev.* **9**, 1455–1476 (2016).

3. J. H. Martin, G. A. Knauer, W. W. Broenkow, VERTEX: the lateral transport of manganese in the northeast Pacific. *Deep Sea Res. Part A, Oceanogr. Res. Pap.* **32** (1985).

4. A. Burd, G. A. Jackson, Predicting particle coagulation and sedimentation rates for a pulsed input. *J. Geophys. Res. Ocean.* **102**, 10545–10561 (1997).

5. A. B. Burd, G. A. Jackson, Particle Aggregation. *Ann. Rev. Mar. Sci.* **1**, 65–90 (2009).

6. A. L. Alldredge, C. Gotschalk, In situ settling behavior of marine snow. *Limnol. Oceanogr.* **33**, 339–351 (1988).

7. lama awawda, Fluid Mechanics Frank White 5th Ed.

8. N. Briggs, G. Dall'Olmo, H. Claustre, Major role of particle fragmentation in regulating biological sequestration of CO2 by the oceans. *Science (80-.).* **367**, 791–793 (2020).

9. A. L. Alldredge, T. C. Granata, C. C. Gotschalk, T. D. Dickey, The physical strength of marine snow and its implications for particle disaggregation in the ocean. *Limnol. Oceanogr.* **35**, 1415–1428 (1990).

10. L. Dilling, A. L. Alldredge, Fragmentation of marine snow by swimming macrozooplankton: A new process impacting carbon cycling in the sea. *Deep. Res. Part I Oceanogr. Res. Pap.* **47**, 1227–1245 (2000).

11. M. H. Iversen, *et al.*, Sinkers or floaters? Contribution from salp pellets to the export flux during a large bloom event in the Southern Ocean. *Deep. Res. Part II Top. Stud. Oceanogr.* **138**, 116–125 (2017).

12. J. H. Cohen, R. B. Forward Jr, "Zooplankton Diel Vertical Migration ‚Äî A Review Of Proximate Control" in (2009), pp. 77–109.

13. D. Bianchi, E. D. Galbraith, D. A. Carozza, K. A. S. Mislan, C. A. Stock, Intensification of open-ocean oxygen depletion by vertically migrating animals. *Nat. Geosci.* **6**, 545–548 (2013).

14. S. M. Bollens, G. Rollwagen-Bollens, J. A. Quenette, A. B. Bochdansky, Cascading migrations and implications for vertical fluxes in pelagic ecosystems. *J. Plankton Res.* **33**, 349–355 (2011).

15. L. Dzierzbicka-Głowacka, Encounter rates in zooplankton. *Polish J. Environ. Stud.* **15**, 243–257 (2006).

16. T. Kiørboe, B. Mackenzie, Turbulence-enhanced prey encounter rates in larval fish: Effects of spatial scale, larval behaviour and size. *J. Plankton Res.* **17**, 2319–2331 (1995).

17. I. J. Alonso-Gonzalez, *et al.*, Role of slowly settling particles in the ocean carbon cycle. *Geophys. Res. Lett.* **37** (2010).

18. A. M. P. McDonnell, K. O. Buesseler, Variability in the average sinking velocity of marine particles. *Limnol. Oceanogr.* **55**, 2085–2096 (2010).

19. N. Briggs, G. Dall'Olmo, H. Claustre, Major role of particle fragmentation in regulating biological sequestration of CO2 by the oceans. *Science (80-.).* **367**, 791–793 (2020).

20. H. Ploug, M. H. Iversen, G. Fischer, Ballast, sinking velocity, and apparent diffusivity within marine snow and zooplankton fecal pellets: Implications for substrate turnover by attached bacteria. *Limnol. Oceanogr.* **53**, 1878–1886 (2008).

21. S. ichi Uye, K. Kaname, Relations between fecal pellet volume and body size for major zooplankters of the Inland Sea of Japan. *J. Oceanogr.* **50**, 43–49 (1994).

22. D. J. Burdige, Preservation of organic matter in marine sediments: Controls, mechanisms, and an imbalance in sediment organic carbon budgets? *Chem. Rev.* **107**, 467–485 (2007).

23. J. J. Middelburg, A simple rate model for organic matter decomposition in marine sediments. *Geochim. Cosmochim. Acta* **53**, 1577–1581 (1989).

24. S. Katsev, S. A. Crowe, Organic carbon burial efficiencies in sediments: The power law of mineralization revisited. *Geology* **43** (2015).

25. J. I. Hedges, R. G. Keil, Sedimentary organic matter preservation: an assessment and speculative synthesis. *Mar. Chem.* **49**, 81–115 (1995).

26. G. Hulthe, S. Hulth, P. O. J. Hall, Effect of oxygen on degradation rate of refractory and labile organic matter in continental margin sediments. *Geochim. Cosmochim. Acta* **62**,

1319–1328 (1998).

27. D. E. Canfield, Factors influencing organic carbon preservation in marine sediments. *Chem. Geol.* **114**, 315–329 (1994).

28. G. L. Cowie, J. I. Hedges, F. G. Prahl, G. J. de Lance, Elemental and major biochemical changes across an oxidation front in a relict turbidite: An oxygen effect. *Geochim. Cosmochim. Acta* **59**, 33–46 (1995).

29. M. Y. Sun, S. G. Wakeham, C. Lee, Rates and mechanisms of fatty acid degradation in oxic and anoxic coastal marine sediments of Long Island Sound, New York, USA. *Geochim. Cosmochim. Acta* **61**, 341–355 (1997).

30. F. Ø. Andersen, Fate of organic carbon added as diatom cells to oxic and anoxic marine sediment microcosms. *Mar. Ecol. Prog. Ser.* **134**, 225–233 (1996).

31. J. A. Cram, *et al.*, The Role of Particle Size, Ballast, Temperature, and Oxygen in the Sinking Flux to the Deep Sea. *Global Biogeochem. Cycles* **32**, 858–876 (2018).

32. A. V. Quinlan, The Thermal Sensitivity of Michaelis-Menten Kinetics as a Function of Substrate Concentration. *J. Franklin Inst.* **310**, 325–342 (1980).

33. A. V. Quinlan, The thermal sensitivity of generic Michaelis-Menten processes without catalyst denaturation or inhibition. *J. Therm. Biol.* **6**, 103–114 (1981).

34. J. M. Arrieta, E. Mayol, R. L. Hansman, G. J. Herndl, Dilution limits dissolved organic carbon utilization in the deep ocean. **348**, 331–334 (2015).

35. J. D. Wilson, S. Arndt, Modeling radiocarbon constraints on the dilution of dissolved organic carbon in the deep ocean. *Global Biogeochem. Cycles* **31**, 775–786 (2017).

36. J. D. Wilson, S. Arndt, Modeling radiocarbon constraints on the dilution of dissolved organic carbon in the deep ocean. 775–786 (2017).

37. H. W. Ducklow, D. A. Hansell, J. A. Morgan, Dissolved organic carbon and nitrogen in the Western Black Sea. *Mar. Chem.* **105**, 140–150 (2007).

38. F. Lopes, *et al.*, Biogeochemical modelling of anaerobic vs. aerobic methane oxidation in a meromictic crater lake (Lake Pavin, France). *Appl. Geochemistry* **26**, 1919–1932 (2011).

39. P. Albéric, E. Viollier, D. Jézéquel, C. Grosbois, G. Michard, Interactions between trace elements and dissolved organic matter in the stagnant anoxic deep layer of a meromictic lake. *Limnol. Oceanogr.* **45**, 1088–1096 (2000).

40. I. Halevy, Production, preservation, and biological processing of mass-independent sulfur isotope fractionation in the Archean surface environment. *Proc. Natl. Acad. Sci. U. S. A.* **110**, 17644–17649 (2013).

41. S. J. Daines, T. M. Lenton, The effect of widespread early aerobic marine ecosystems on methane cycling and the Great Oxidation. *Earth Planet. Sci. Lett.* **434**, 42–51 (2016).

42. S. Q. Lang, D. A. Butterfield, M. D. Lilley, H. Paul Johnson, J. I. Hedges, Dissolved organic carbon in ridge-axis and ridge-flank hydrothermal systems. *Geochim. Cosmochim. Acta* **70**, 3830–3842 (2006).

43. F. C. Wu, R. B. Mills, Y. R. Cai, R. D. Evans, P. J. Dillon, Photodegradation-induced changes in dissolved organic matter in acidic waters. *Can. J. Fish. Aquat. Sci.* **62**, 1019–1027 (2005).

44. D. J. Burdige, W. M. Berelson, K. H. Coale, J. McManus, K. S. Johnson, Fluxes of

dissolved organic carbon from California continental margin sediments. *Geochim. Cosmochim. Acta* **63**, 1507–1515 (1999).

45. M. J. Alperin, *et al.*, Benthic fluxes and porewater concentration profiles of dissolved organic carbon in sediments from the North Carolina continental slope. *Geochim. Cosmochim. Acta* **63**, 427–448 (1999).

46. N. Lahajnar, T. Rixen, B. Gaye-Haake, P. Schäfer, V. Ittekkot, Dissolved organic carbon (DOC) fluxes of deep-sea sediments from the Arabian Sea and NE Atlantic in *Deep-Sea Research Part II: Topical Studies in Oceanography*, (2005), pp. 1947–1964.

47. Z. V. Finkel, "Marine net primary production" in *Global Environmental Change*, (Springer Netherlands, 2014), pp. 117–124.

48. D. W. Folger, Desert Dust: Origin, Characteristics, and Effect on Man. *Eos, Trans. Am. Geophys. Union* **64**, 146 (1983).

49. K. Ozaki, E. Tajika, Biogeochemical effects of atmospheric oxygen concentration, phosphorus weathering, and sea-level stand on oceanic redox chemistry: Implications for greenhouse climates. *Earth Planet. Sci. Lett.* **373**, 129–139 (2013).

50. S. Katsev, D. G. Rancourt, I. L'Heureux, dSED: A database tool for modeling sediment early diagenesis. *Comput. Geosci.* **30**, 959–967 (2004).

Table S1. Parameters for the box model and sensitivity analysis

Parameter	Symbol	Value	Unit	Range	Ref.
Area of surface ocean	$A_{surface}$	3.1×10^8	km^2	-	(40)
Volume of surface ocean	$V_{surface}$	3.3×10^7	km^3	-	(40)
Volume of intermediate ocean	$V_{intermediate}$	3.4×10^8	km^3	-	(40)
Volume of deep ocean	V_{deep}	1.3×10^9	km^3	-	(40)
Area of high-lat. downwelling	A_{dwell}	2.9×10^7	km^2	-	(40)
Volume of high-lat. downwelling	V_{dwell}	2.9×10^7	km^3	-	(40)
Area of high-lat. upwelling	A_{upwell}	2.9×10^7	km^2	-	(40)
Volume of high-lat. upwelling	V_{upwell}	2.9×10^7	km^3	-	(40)
Continental shelf	$A_{continental}$	3.8×10^7	km^2	-	(40)
Continental shelf	$V_{continental}$	3.8×10^6	km^3	-	(40)
Upwelling zones, slope	$A_{upwell,slope}$	1.9×10^7	km^2	-	(40)
Upwelling zones, slope	$V_{upwell,slope}$	1.1×10^6	km^3	-	(40)
Upwelling zones, surface	$A_{upwell,surf}$	1.9×10^7	km^2	-	(40)
Upwelling zones, surface	$V_{upwell,surf}$	1.1×10^6	km^3	-	(40)
Turbulent diffusion exchange surface to continental	K_{21}	20	Sv	-	(40, 41)
Turbulent diffusion exchange surface to intermediate	K_{24}	60	Sv	-	(40, 41)
Turbulent diffusion exchange intermediate to deep	K_{43}	38	Sv	-	(40, 41)
Turbulent diffusion exchange intermediate to upwelling	K_{54}	10	Sv	-	(40)
Advective flux from intermediate to upwelling slope	K_{45}	0.4	Sv	-	(40)

Advective flux from upwelling slope to upwelling surface	K_{56}	0.4	Sv	-	(40)
Advective flux from upwelling surface to surface	K_{62}	0.4	Sv	-	(40)
Diffuse exchange upwelling to deep	K_{83}	48	Sv	-	(40)
DOC hydrothermal flux	F_{Hydro}	1	g C/year	0.7–1.4x10^{10}	(42)
DOC photodegradation rate constant	K_{photo}	0.5	1/day	0.1-1	(43)
DOC half saturation constant	k_{DOC}	150	µM	50-500	(34, 36)
DOC benthic flux coastal sediment	$F_{sed,\ coast}$	500	µmol/m2/day	100 - 1000	(44–46)
DOC benthic flux deep sediment	$F_{sed,\ deep}$	50	µmol/m2/day	10 - 100	(44–46)

Table S2. Range of parameters used in the biological carbon pump model and its sensitivy analysis (SA). The full description of the model along with the results of the sensitivity analysis are described in (1).

Parameter	Symbol	Value	Unit	Range used in the SA
Net primary production flux	F_{NPP}	0.06	gC m^{-2} yr^{-1}	100-400 (47)
Dust flux	F_{Dust}	0.04	Pg yr^{-1}	0.01-0.1 (48)
Calcite flux	F_{Ca}	0.01	Pg yr^{-1}	0.005-0.05
Silica flux	*Fsilica*	0.005	Pg yr^{-1}	0.001-0.01
Mixing depth	L_{mix}	200	m	200-400
Temperature dependency factor	Q_{10}	1	-	1.2-2.2 (32, 33)
Depth scale for thermocline	L_{thermo}	800	m	800-1200
Reference temperature	*Tref*	4	^{o} C	4-25
Aggregation efficiency factor	K_{aggr}	0.5	-	0.1-1
Fractal dimension	D_N	2	-	1.3-3 (2)
Seawater surface temperature	*SST*	25	^{o} C	4-35
Seawater surface density	*SSD*	1.0255	g/cm^3	1.0253-1.026
Fraction of NPP by picoplankton	f_{Pi}	0.75	-	0.4 - 0.9
Fraction of NPP by coccolithophorid	f_C	0.1	-	0 – 0.3
Fraction of NPP by Aragonite forming phytoplankton	f_A	0.1	-	0 – 0.3
Fraction of NPP by diatom	f_{Di}	0.05	-	0 – 0.15
Stefan–Boltzman constant	k_{Boltz}	1.380 x10^{-23}	m^2 kg s^{-2} K^{-1}	
Reference value for collision rate	β_{ref}	1x10^{-15}	m^3/s	1x10^{-15}- 1x10^{-12}
Turbulent dissipation rate	ε	1×10^{-4}	m^2/s^3	1×10^{-5} - 1×10^{-3} (2)
Prosome length (small zooplankton)	*PL*	-	µm	100-500 (21)
Prosome length (large zooplankton)	*PL*	-	µm	300-2000 (21)
Turbulent velocity	*w*	1	m/s	10-25 (15)
Zooplankton velocity (small zooplankton)	*v*	-	m/d	100 - 1000
Zooplankton velocity (large zooplankton)	*v*	-	m/d	1000 - 6000
Eddy diffusion coefficient at the surface	$K_{z,\,surf}$	5×10^{-3}	m^2/s	10^{-3} - 10^{-2} (49)
Eddy diffusion coefficient at the thermocline	$K_{z,\,therm}$	6×10^{-4}	m^2/s	10^{-4} - 10^{-3} (49)
Eddy diffusion coefficient in the deep ocean	$K_{z,\,depp}$	6×10^{-3}	m^2/s	10^{-3} - 10^{-2} (49)
Monod constant for O_2	K_i	2	μM	1 – 2 (50)
Iron oxidation rate constant	k_{fe}	100	1/µM/year	100-500 (50)

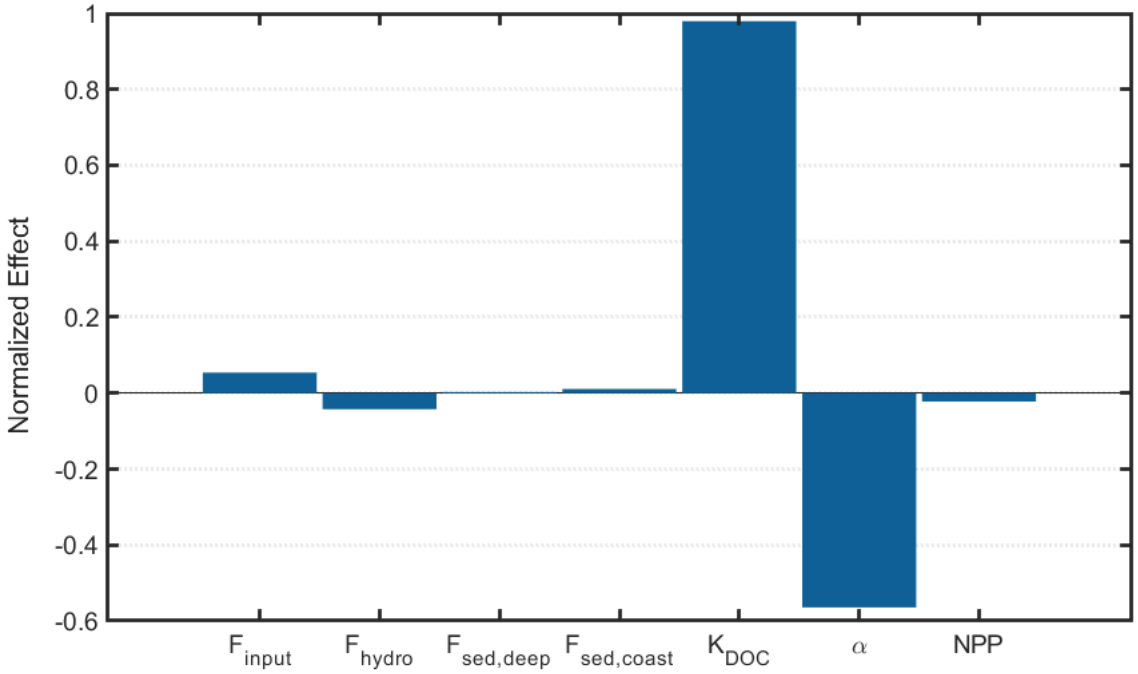

Figure S1. *Results of the analysis of the sensitivity of modeled marine DOC concentration to variation of input parameters. For easier comparison, the percentage change in the average DOC concentration in response to a change in the model parameters was normalized to the percetange change of the model parameter. Based on the results of the sensitivity analysis, the DOC half-saturation constant, k_{DOC}, exerts the strongest leverage on the DOC concentration of the oceans. An increase in k_{DOC} would decrease the overall rate of DOC consumption by heterotrophs, resulting in a higher marine DOC concentration.*

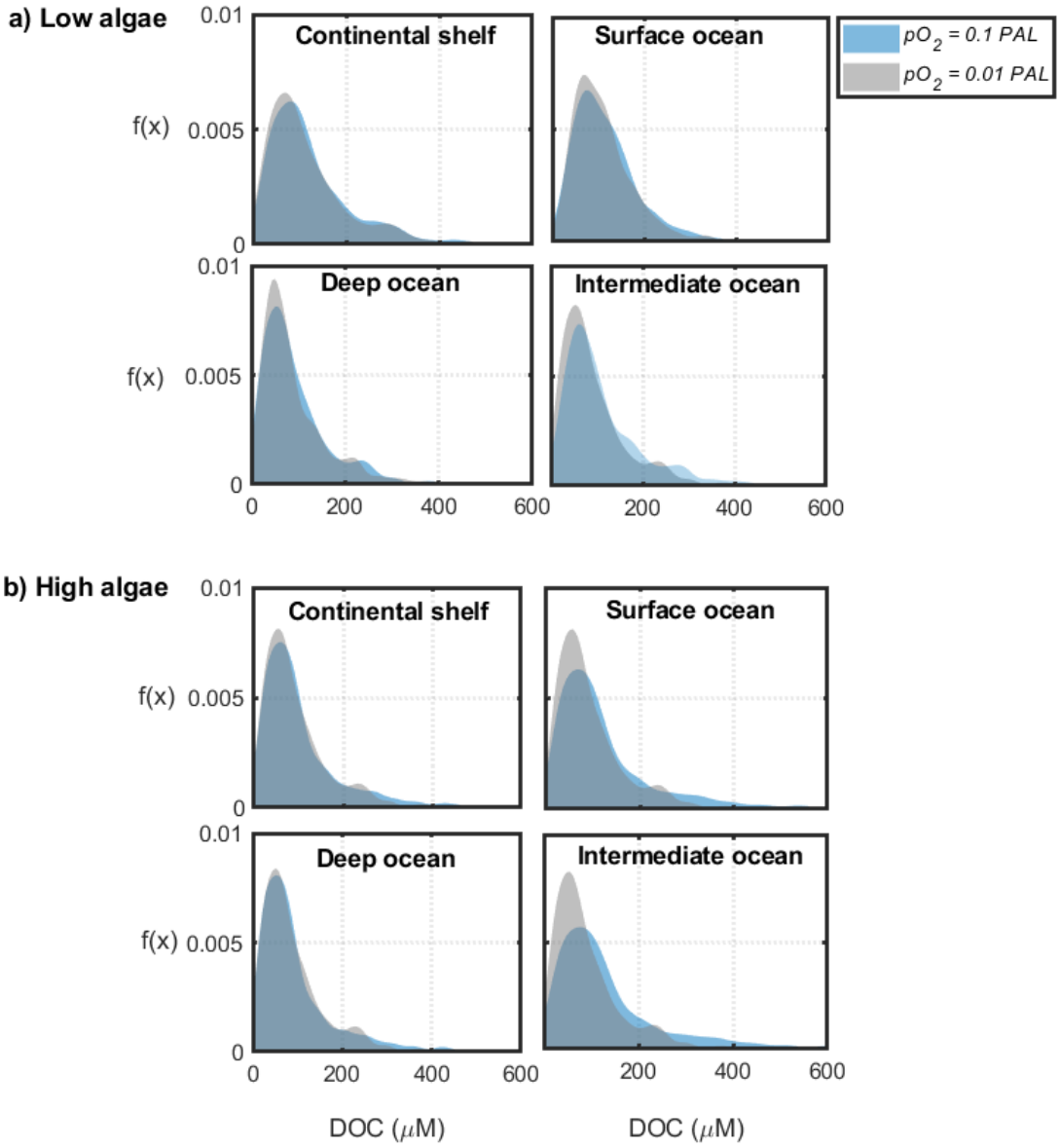

Figure S2*. Effect of the evolution of algae and atmospheric oxygen concentration on marine DOC concentrations. Results for marine DOC concentration with low-algae (<10% contribution of algae to marine primary production) and high-algae conditions (>90% contribution of algae to marine primary production) under different atmospheric oxygen levels of 0.01 and 0.1 present atmospheric level (PAL) are, respectively, presented in panels (a) and (b). The change in the contribution of algae to marine primary production has little impact on overall marine DOC concentrations under different atmospheric oxygen levels.*

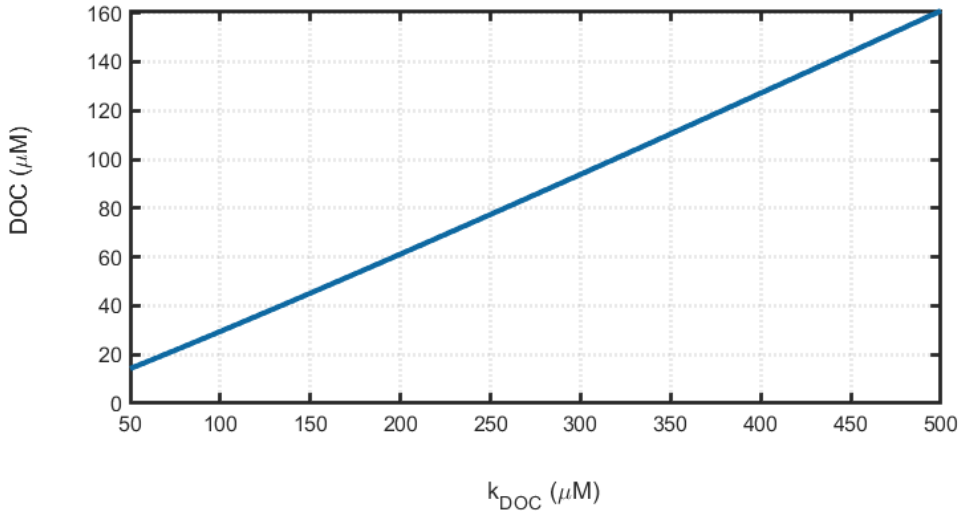

Figure. S3*. The effect of the DOC uptake threshold (k_{DOC}) on steady-state DOC concentration in the deep-ocean box.*

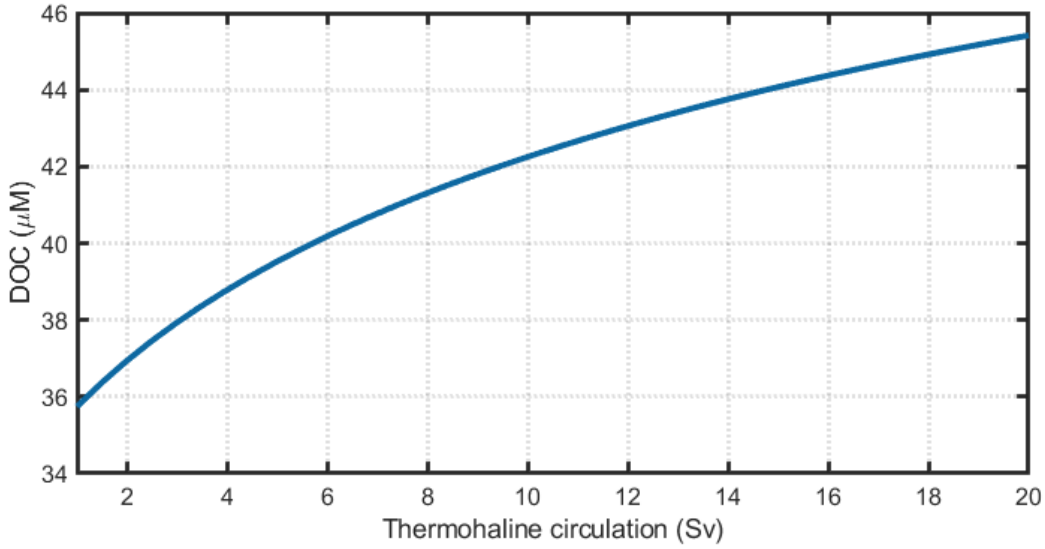

Figure. S4*. The effect of the strength of oceanic circulation on steady-state DOC concentration in the deep-ocean box.*